Available online at www.sciencedirect.com
SCIENCE DIRECT®
Journal of Power Sources 128 (2004) 173–184
JOURNAL OF POWER SOURCES
www.elsevier.com/locate/jpowsour

A two-dimensional computational model of a PEMFC with liquid water transport

N.P. Siegel, M.W. Ellis*, D.J. Nelson, M.R. von Spakovsky

Department of Mechanical Engineering, Virginia Polytechnic and State University, Blacksburg, VA, USA

Received 27 August 2003; accepted 20 September 2003

Abstract

A comprehensive, steady-state, computational model of a proton exchange membrane fuel cell (PEMFC) derived from first principles is presented. The model is two-dimensional and includes the transport of liquid water within the porous electrodes as well as the transport of gaseous species, protons, energy, and water dissolved in the ion conducting polymer. Electrochemical kinetics are modeled with standard rate equations adapted to an agglomerate catalyst layer structure. Some of the physical properties used in constructing the model are determined experimentally for an in-house membrane electrode assembly (MEA) and are presented herein. Experimental results obtained for the MEA are used to validate the computational model. Modeling results are presented that illustrate the importance of the transport of water within the porous sections of the cell and in the polymer regions of the MEA.

Keywords: Computational model; PEMFC; Proton exchange membrane; Water transport; Agglomerate

1. Introduction

The development of economical, commercially available proton exchange membrane (PEM) fuel cells is essential to the development of a hydrogen based energy infrastructure. The PEM fuel cell is particularly important to the development of hydrogen fueled vehicles as demonstrated by the fact that all of the major automobile manufacturers are currently involved in some level of PEM fuel cell research with the goal of widespread commercialization within 10–15 years. To realize this and other development goals, fuel cell technology must continue to improve with respect to cost and performance. Computational models of fuel cells can contribute to this effort by providing researchers with the ability to create and optimize fuel cell designs rapidly and inexpensively before actually building a prototype.

1.1. Overview of fuel cell models

The need for computational tools to support the design process has led to the development of a number of fuel cell models. These models can generally be characterized by the scope of the model. In many cases, modeling efforts focus on a specific part or parts of the fuel cell, like the cathode catalyst layer [1–4], the cathode electrode (gas diffusion layer plus catalyst layer) [5], or the membrane electrode assembly (MEA) [6,7]. These models are very useful in that they may include a large portion of the relevant fuel cell physics while at the same time having relatively short solution times. However, these narrowly focused models neglect important parts of the fuel cell making it impossible to get a complete picture of the phenomena governing fuel cell behavior. Models that include all parts of a fuel cell are typically two- or three-dimensional and reflect many of the physical processes occurring within the fuel cell [8–12]. Comprehensive models rely on the determination of a large number of properties and operating parameters and can be much more computationally intensive, leading to longer solution times. However, these disadvantages are typically outweighed by the benefit of being able to assess the influence of a greater number of design parameters and their associated physical processes. The model presented in this work is a comprehensive two-dimensional model that includes multicomponent and multiphase transport both along the flow direction (down the gas channel) and through the MEA.

1.2. Models of liquid water transport

A comprehensive computational model should include the equations and other numerical relations needed to fully define fuel cell behavior over the range of interest. Early

* Corresponding author. Tel.: +1-540-231-9102; fax: +1-540-231-9100.
E-mail address: mwellis@vt.edu (M.W. Ellis).

0378-7753/$ – see front matter © 2003 Elsevier B.V. All rights reserved.
doi:10.1016/j.jpowsour.2003.09.072

Nomenclature

Parameters and variables

c	concentration (mol/mm^3)
c_{eff}	effective heat capacity (J/g K)
D	diffusivion coefficient (mm^2/s)
E_{th}	Nernst potential (V)
F	Farraday's constant
h_{fg}	enthalpy of vaporization (J/g)
k_{eff}	effective thermal conductivity (W/mm K)
M	molar mass (g/mol)
n	number of electrons
P	pressure (Pa)
R	universal gas constant (J/mol K)
s	saturation
s_{f}^{o}	standard entropy of formation (J/mol K)
S	source term—see Table 2
t	thickness (mm)
T	temperature (K)
u	velocity (mm/s)
V_{cell}	cell voltage (V)
w	mass fraction

Greek letters

ϕ	potential (V)
ε	volume fraction
γ	switch function
κ	relative humidity
λ	polymer water content H_2O/SO_3^-
μ	viscosity (Pa s)
ρ	density (g/mm^3)
σ	ionic conductivity (Ω mm)$^{-1}$
τ	tortuosity

Subscripts

a	anode
act	activation
c	cathode
C	carbon
coll	current collector
d	index for electrodes (anode: $d = a$, cathode: $d = c$)
drag	electro-osmotic drag
Dar	Darcy pressure loss
eff	effective
evap	evaporation
H_2	hydrogen
i	ionic
LV	mass transfer from liquid to vapor
O_2	oxygen
p	polymer
pl	plate
rev	reversible heat
v	vapor
void	void space
W	water
WD	water dissolved in polymer
WV	water vapor
WL	water liquid
WP	water production
x	x-direction – through MEA
y	y-direction – down channel
Ω	Ohmic

Superscripts

cat	catalyst layer
cp	capillary pores
g	gas phase
gdl	gas diffusion layer
p	polymer phase
v	vapor phase

multidimensional models described gas transport in the flow channels, gas diffusion layers (GDLs), and the membrane [11,10]. More recent models include a detailed description of the catalyst layers that reflects the agglomerate nature of these regions [12]. Recently, there has been an interest in describing operating regimes that are dominated by mass transport limitations resulting, in part, from the formation and transport of liquid water within the fuel cell. To model fuel cell performance in these regimes, it is necessary to include equations that describe not only the motion of water within the liquid phase, but also mass transfer between phases. He et al. [15] present a model for liquid water transport in the cathode gas diffusion layer of a fuel cell with an interdigitated flowfield. As part of their work they formulate a switching function that is used to toggle source terms on and off depending on whether water is condensing into the liquid phase or evaporating into the vapor phase. They also introduce a term to account for water transport by advection, or transport due to the motion of the bulk flow, which is an important transport mechanism for interdigitated flowfields. In a continuation of this work, Natarajan and Nguyen [16] develop a diffusive expression to account for water transport via capillary pressure in the porous electrode. They neglect water transport by advection since their model uses a conventional flowfield. Wang and Wang [17] have also developed a model for two phase flow in an interdigitated cathode. They assume transport by capillary pressure only and do not include mass transport between phases. All three of these models treat the catalyst layer as an interface and so do not consider effects due to water buildup within the catalyst layer. The model of Baschuk and Li [18] is one-dimensional and includes liquid water effects in both the gas diffusion layer and the catalyst layer. In the Baschuk and Li model, phase change is neglected and the volume fraction of liquid water in the porous regions must be specified as opposed to being calculated.

1.3. Determination of physical properties

Another important part of developing a useful computational fuel cell model is the accurate determination of the physical properties on which the model is based. These properties may include: porosity of the gas diffusion layer and catalyst layer; the ionic conductivity of the polymer membrane; mass transfer coefficients; kinetic parameters such as the exchange current density and reaction surface area; and structural properties such as the thicknesses of the catalyst layers, membrane, and gas diffusion layers. Many of these properties can be experimentally determined with considerable accuracy. Others, like interphase mass transfer coefficients, are more difficult to determine and must be estimated. In either case, it is important to take great care with the values used as they may significantly affect the results [1].

Prior research has determined many of the physical properties needed for modeling. The work by Parthasarathy et al. [13] and Zhang et al. [19] contains experimentally determined values for many of the kinetic parameters involved with the oxygen reduction reaction occurring at the cathode as well as data regarding the solubility and diffusivity of oxygen in Nafion®. Ihonen et al. [14] present data for the pore size distribution and porosity of the catalyst layer. In their work, they compare the pore size distribution as determined by both gas and mercury porosimetry and show that the two methods provide nearly identical results for the catalyst layers that they tested. Many of the required properties for Nafion® 1100, including ionic conductivity and the electro-osmotic drag coefficient, can be found in the work by Springer et al. [6]. Marr and Li [2] present data for catalyst surface area as it relates to the type of catalyst used in the MEA. This data is for a perfectly uniform catalyst deposition. However, transmission electron microscope (TEM) images such as those shown by Siegel et al. [12] reveal that the catalyst deposition is not uniform and property data must be modified to account for the effect of catalyst non-uniformities. In the current work, we experimentally determine the catalyst layer porosity and thickness using a scanning electron microscope (SEM) and the reaction surface area using cyclic voltammetry.

1.4. Characteristics of present model

The present work presents a comprehensive model of a PEM fuel cell that incorporates the significant physical processes and the key parameters affecting fuel cell performance. The model is two-dimensional and includes the transport of gaseous species, protons, energy, and water dissolved in the ion conducting polymer. The model also addresses the transport of liquid water within the fuel cell with liquid water assumed to be transported by capillary pressure within the gas diffusion layers and catalyst layers and by advection within the gas channels. Water is assumed to be exchanged among three phases—liquid, vapor, and dissolved[1]—and equilibrium among these phases is assumed. Electrochemical kinetics are modeled with standard rate equations adapted to an agglomerate catalyst structure. The model reflects the influence of numerous parameters on fuel cell performance including geometry, porosity of the cell materials, catalyst area, polymer properties, catalyst layer composition, and others. This paper describes the development of the model, the determination of properties for use in the model, the validation of the model using experimental data, and the application of the model to explain observed experimental phenomena.

2. Model development

Fig. 1 shows the solution domain of the model. In the anode and cathode gas channels, fuel and oxidant flow along the surface of the membrane electrode assembly. In these regions, the flow is considered to be laminar. Reactants move from the gas channels into the gas diffusion layers (GDL) which serve to more uniformly distribute the reactants across the surface of the catalyst layer. In the catalyst layers, the reactants are transported by diffusion and advection while participating in electrochemical reactions. The polymer membrane is assumed to transport only protons and dissolved water. The current collector plates are not explicitly included in the computational model. Their influence with respect to energy transport is included and discussed in the next section.

2.1. Governing equations

The governing equations include conservation of mass, momentum, ionic charge, and energy as well as individual species conservation equations. The governing equations are presented in Table 1. Related terms that describe the rate at which the conserved quantity is added or removed from the solution domain are referred to as “source” terms and are presented in Table 2. Constitutive relations describing reaction rates, polymer properties, gas properties, and liquid properties are provided in Table 3.

Each of the governing equations is developed for the entire solution domain of the model with source and transport terms modified in each region to reflect the appropriate physical phenomena. Eq. (1) describes conservation of mass for the entire gas phase. Source terms reflect changes in the overall gas phase mass flow due to consumption or production of gas species via reaction and due to mass transfer between water in the vapor phase and water that is in the liquid phase or dissolved in the polymer. The system of equations that model the interphase mass transfer is described in more detail in the following section. The gas phase mixture density is determined from the temperature, pressure,

[1] Here, “dissolved” refers to water that exists within the polymer membrane or the polymer phase of the catalyst layer.

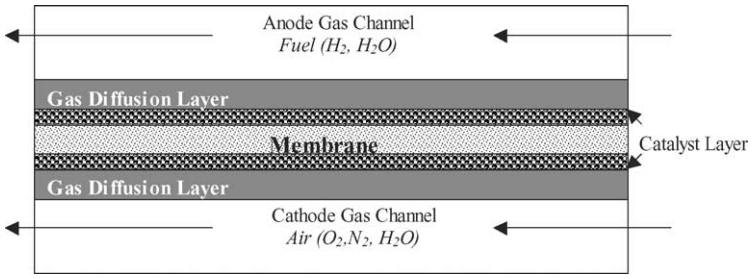

Fig. 1. Solution domain.

Table 1
Governing equations

Conservation equation	General form of equation	
Mass	$\nabla \cdot (\rho^{g}\bar{u}) = S_{H_2} + S_{O_2} + S_{LV} + S_{WP}\gamma_{LV} - S_{WD}\gamma_{WD}$	(1)
Momentum	$\bar{u} \cdot \nabla[\rho^{g}u_x] = -\dfrac{\partial P}{\partial x} + \mu\nabla^2 u_x + S_{Dar,x}$	(2a)
	$\bar{u} \cdot \nabla[\rho^{g}u_y] = -\dfrac{\partial P}{\partial y} + \mu\nabla^2 u_y + S_{Dar,y}$	(2b)
Oxygen	$\rho^{g}\bar{u} \cdot \nabla w_{O_2} + w_{O_2}\nabla \cdot (\rho^{g}\bar{u}) = \nabla \cdot (D^{g}_{O_2}\rho^{g}\nabla w_{O_2}) + S_{O_2}$	(3)
Water vapor	$\rho^{g}\bar{u} \cdot \nabla w_{WV} + w_{WV}\nabla \cdot (\rho^{g}\bar{u}) = \nabla \cdot (D^{g}_{WV}\rho^{g}\nabla w_{WV}) + S_{LV} + S_{WP}\gamma_{LV} - S_{WD}\gamma_{WD}$	(4)
Liquid water	$\bar{u} \cdot \nabla s = \nabla \cdot (D^{cp}_{WL}\nabla s) - \dfrac{S_{LV}}{\rho_{WL}} + \dfrac{S_{WP}(1-\gamma_{LV})}{\rho_{WL}} - \dfrac{S_{WD}(1-\gamma_{WD})}{\rho_{WL}}$	(5)
Dissolved water	$-\dfrac{2.5}{22F}\nabla \cdot (\lambda\varepsilon_p\sigma_i\nabla\phi_i) = \nabla \cdot (D^{p}_{WD}\nabla c^{p}_{WD}) + \dfrac{S_{WD}}{M_W}$	(6)
Ionic charge	$\nabla \cdot (\varepsilon_p\sigma_i\nabla\phi_i) + S_i = 0$	(7)
Thermal energy	$\rho^{g}c_{eff}\bar{u} \cdot \nabla T = \nabla \cdot (k_{eff}\nabla T) + S_\Omega + S_{rev} + S_{act} + S_{pc} + S_{pl}$	(8)

Table 2
Source terms

Source term (region of application − zero in other regions)	Defining equation	
Darcy pressure drop in the x-direction (Pa/mm) (anode and cathode GDLs and catalyst layers)	$S_{Dar,x} = -\dfrac{\mu}{\kappa}u_x$	(9)
Darcy pressure drop in the y-direction (Pa/mm) (anode and cathode GDLs and catalyst layers)	$S_{Dar,y} = -\dfrac{\mu}{\kappa}u_y$	(10)
Hydrogen reaction rate (g/mm^3 s) (anode catalyst layer)	$S_{H_2} = -\dfrac{M_{H_2}}{2F}\lvert R_{eff,a}\rvert$	(11)
Oxygen reaction rate (g/mm^3 s) (cathode catalyst layer)	$S_{O_2} = -\dfrac{M_{O_2}}{4F}\lvert R_{eff,c}\rvert$	(12)
Water production rate (g/mm^3 s) (cathode catalyst layer)	$S_{WP} = \dfrac{M_W}{2F}\lvert R_{eff,c}\rvert$	(13)
Mass transfer rate from liquid to vapor (g/mm^3 s) (anode and cathode cat. layers, GDLs, gas channels)	$S_{LV} = \psi s\gamma_{LV} - \psi(1-s)(1-\gamma_{LV})$	(14)
Mass transfer rate into the dissolved phase (g/mm^3 s) (anode and cathode catalyst layers)	$S_{WD} = h_m(\rho^{g}_{WV} - \rho^{p}_{WV})$	(15)
Ionic current generation (A/mm^3) (anode and cathode catalyst layers)	$S_i = R_{eff,d}\begin{cases} +\text{ at anode (d = a)} \\ -\text{ at anode (d = c)} \end{cases}$	(16)
Heat source due to ohmic heating, (anode and cathode catalyst layers; membrane)	$S_\Omega = \nabla\phi_i \cdot (\varepsilon_p\sigma_i\nabla\phi_i)$	(17)
Heat source due to reversible chemical reaction (anode and cathode catalyst layers)	$S_{rev} = \dfrac{R_{eff,k}T}{n_k F}\sum_{p-r} s^{o}_{f,k}$	(18)
Heat source due to activation loss (W/mm^3) (anode and cathode catalyst layers)	$S_{act} = (\phi_{e,d} - \phi_i)R_{eff,k}$	(19)
Heat source due to phase change (W/mm^3) (cathode catalyst layer)	$S_{pc} = (-S_{LV} + S_{DW}\gamma_{DW})h_{fg}$	(20)
Heat source due to the current collector plate (W/mm^3) (anode and cathode GDLs)	$S_{pl} = \dfrac{(T_{coll} - T)}{t_{gdl}}\left(\dfrac{t_{gdl}}{k_{gdl}} + \dfrac{t_{coll}}{k_{coll}}\right)^{-1}$	(21)

Table 3
Closure relations

Parameter	Defining equation	
Reaction rate equations (anode: d = a, k = H_2, $n_{H_2} = 1$; cathode: d = c, k = O_2, $n_{O_2} = 1$)		
Effective reaction rate, R_{eff} (A/mm^3)	$R_{eff,d} = R_d \eta_{aggl,d}$	(22)
Reaction rate, R (A/mm^3)	$R_d = (1-s) A_{pv} i_{o,k} \left(\frac{c_k^p}{c_{k,ref}}\right)^{\gamma} \left[e^{(\phi_{e,d}-\phi_i)\alpha_d (n_d F/RT)} - e^{-(\phi_{e,d}-\phi_i)\alpha_d (n_d F/RT)}\right]$	(23)
Electrical potential, ϕ_e	$\phi_{e,a} = 0$ $\phi_{e,c} = -(E_{th} - V_{cell})$	(24)
Agglomerate effectiveness, η_{aggl}	$\eta_{aggl,d} = \frac{3}{\beta_d}\left(\frac{1}{\tanh(\beta_d)} - \frac{1}{\beta_d}\right)$	(25)
Thiele's modulus, β	$\beta_d = L_{aggl,d}\sqrt{\frac{\lvert R_d \rvert}{c_k^p D_k^p n_d F}}$	(26)
Dissolved gas concentration, c_k^p (mol/mm^3)	$c_k^p = h_k^p c_k^g T$	(27)
Material properties		
Polymer water content, λ (mol-W/mol-p)	$\lambda = \frac{c_{DW}^p M_p}{\rho_m}$	(28)
Ionic conductivity of the polymer, σ_i (S/mm)	$\sigma_i = (0.0005139\lambda - 0.000326)\exp\left[1268.0\left(\frac{1}{303} - \frac{1}{T}\right)\right]$	(29)
Water diffusivity in the polymer, D_{DW}^p (mm^2/s)	$D_{DW}^p = 1.3\times10^{-4}\exp\left[2416\left(\frac{1}{303} - \frac{1}{T}\right)\right]$	(30)
Water vapor activity, a	$a = 1.76\,e^{-6}\lambda^4 + 2.17\,e^{-4}\lambda^3 - 8.80\,e^{-3}\lambda^2 + 0.16\lambda - 0.12$	(31)
Density of water vapor in equilibrium with the polymer, $\rho_{WV}{}^p$ (g/mm^3)	$\rho_{WV}^p = \rho_{SAT}^g \cdot a$	(32)
Gas density, ρ^g (g/mm^3)	$\rho^g = \frac{P}{RT\sum(w_j/M_j)}$	(33)
Gas component diffusivity (mm^2/s)	$D_k^g = \frac{\rho^g(1-y_k)}{\sum_{j\neq k}(y_j/D_{jk})}$ gas channel	(34a)
	$D_{eff,k}^g = \frac{D_k^g \varepsilon_{void}^{gdl}(1-s)}{\tau^{gdl}}$ porous GDL	(34b)
	$D_{eff,k}^g = D_k^g[\varepsilon_{void}^{gdl}(1-s)]^{1.5}$ porous catalyst layer	(34c)
Capillary diffusivity, D_{WL}^{cp} (mm^2/s)	$D_{WL}^{cp} = \frac{\rho_{WL} g}{\mu_{WL}} K(s)\frac{\partial P_c}{\partial s}$	(35a)
	$K(s)\frac{\partial P_c}{\partial s} = 0.0155s^3 - 0.0213s^2 + 0.0088s + 0.0002$	(35b)
Effective thermal conductivity of region r (W/mm K)	$k_{eff} = \varepsilon_{void}^r(1-s)k_g + \varepsilon_{void}^r s k_{WL} + \varepsilon_p^r k_p + \varepsilon_c^r k_c$	(36)
Equilibrium control functions		
Liquid/vapor switch, γ_{LV} $\gamma_{LV}\to 1$ for $\frac{\rho_{WV}^g}{\rho_{SAT}^g} < 0.98$, else 0	$\gamma_{LV} = 1 - 0.5\left[1 + \tanh\left(61\frac{\rho_{WV}^g}{\rho_{SAT}^g} - 59\right)\right]$	(37)
Dissolved water switch, γ_{WD} $\gamma_{WD} = 1$ for $\rho_{WV}^p < \rho_{WV}^g$, else 0	$\gamma_{WD} = 0.5 + \frac{\rho_{WV}^g - \rho_{WV}^p}{2\lvert\rho_{WV}^g - \rho_{WV}^p\rvert}$	(38)

and mixture molar mass using the ideal gas equation, Eq. (33).

Conservation of momentum is expressed by the Navier–Stokes equations in vector form, Eqs. (2a) and (2b), which are modified by source terms described by Eqs. (9) and (10) to account for Darcy flow in the porous regions of the model. The Darcy terms are active in the GDLs and catalyst layers only; the inertial and bulk viscous terms are neglected in these regions.

The species equations for oxygen and water vapor are given by Eqs. (3) and (4), respectively. For both the anode and cathode sides of the cell, the number of species equations is one less than the number of species. At the anode, the species equation for water vapor is solved. The hydrogen mass fraction is calculated from the solution to the water vapor equation and the overall gas phase conservation equation. At the cathode, both water vapor and oxygen species equations are solved. The nitrogen mass fraction is determined from the solutions to these species equations and the overall gas phase conservation equation. The diffusion of each species within the bulk flow is given by the first term on the right side. The diffusion coefficients for multi-component flow, which are determined by Eqs. (34a)–(34c), are based on a simplification of the

Stefan-Maxwell equations and in porous regions are modified by porosity and tortuosity factors [9,22]. The advective term for each of the species equations is separated into two parts. The first is equal to the product of velocity, mixture density, and mass fraction gradient. The second term is the product of mass fraction and the divergence of total mass flux. For the oxygen species equation, Eq. (3), the consumption of oxygen via reaction is reflected in the source term given by Eq. (12). The water vapor transport equation, Eq. (4), reflects the movement of water vapor by diffusion and bulk motion; the exchange of water between the vapor phase and the liquid phase is given by Eq. (14); the exchange of water between the vapor phase and the dissolved phase by Eq. (15); and the production of water by Eq. (13).

Liquid water transport within the cell is modeled with Eq. (5). The variable that describes liquid water is the saturation, s, which is the volume fraction of liquid water relative to the pore volume in the porous sections of the fuel cell, i.e.

$$s \equiv \frac{V_{\mathrm{WL}}}{V_{\mathrm{pore}}} \tag{39}$$

Within the porous electrodes, liquid water is transported by capillary pressure and interphase mass transfer. The bulk flow term is neglected. The diffusion coefficient for liquid water, $D_{\mathrm{WL}}^{\mathrm{cp}}$, accounts for water motion via capillary pressure and is based on a semi-empirical relation between capillary pressure and saturation [16]. Within the gas channels, capillary effects are neglected and the liquid is assumed to travel as droplets of negligible volume with a velocity that is equal to the bulk gas velocity. Water is exchanged with the liquid phase, due to evaporation into the vapor, as given by Eq. (14); production from the cathode reaction as given by Eq. (13) if the adjacent vapor is saturated; and transfer into the liquid from the dissolved phase as given by Eq. (15). Equilibrium between the various water phases is described in more detail in Section 2.2.

Water in the dissolved form is transported within the polymer membrane and the polymer phase of the catalyst layer as described by Eq. (6). The transport mechanisms include diffusion, electro-osmotic drag, and inter-phase mass transfer as defined by Eq. (15). An advective term would be required if the gas pressure in the anode differed significantly from that in the cathode. For this model, the anode and cathode pressures are assumed to be equal and so the convective transport of water through the MEA is neglected. The transport of ions in the polymer regions of the fuel cell is described by Eq. (7), where the source term, Eq. (16), represents the production/consumption of protons via the electrochemical reactions in the catalyst layers.

The rate of the electrochemical reaction is described by Eqs. (22) and (23) which represent a form of the Butler–Volmer relation modified by an effectiveness factor to account for the effect of diffusion through the agglomerate structures in the catalyst layer and multiplied by the term $(1 - s)$ to account for the occlusion of reaction sites due to the accumulation of liquid water within the cell [17]. The effectiveness term, given by Eq. (25), is a measure of how readily reactants diffuse through the spherical agglomerates. An effectiveness of 1.0 indicates that reactants diffusing through the agglomerates encounter no resistance. An effectiveness less than 1.0 indicates that the agglomerate offers resistance to reactant diffusion thereby limiting the reaction rate. The rate of reaction is controlled by the reactant concentration in the polymer at the interface with the reactant gas as given by Henry's law, Eq. (27), and by the local activation overpotential given by $(\phi_{\mathrm{e,d}} - \phi_{\mathrm{i}})$. The electrical potential is assumed to be constant over each electrode (catalyst and GDL). As indicated by Eq. (24), the electrical potential is set to zero on the anode side and to the negative of the total overvoltage on the cathode side.

Conservation of thermal energy is expressed by Eq. (8) and reflects heat transfer by conduction and convection as well as source terms for Ohmic heating due to ionic resistance as given by Eq. (17), reversible heat as defined by Eq. (18), heat produced via activation losses as given by Eq. (19), and the latent heat associated with the phase change of water as given by Eq. (20). In this model, the collector plates are not included in the solution domain. In an actual fuel cell, the shoulder of the plates would be in contact with the MEA and provide a low-resistance pathway for heat. The source term, S_{pl}, which is given by Eq. (21) approximates the heat transfer through the collector plates had they been part of the solution domain.

2.2. Mass transfer between dissolved, liquid, and vapor phases

The model presented here assumes that the three phases in which water can exist—liquid, vapor, and dissolved—are in equilibrium. With this assumption, the model does not address the actual rate of transport between the three phases or the actual path the water follows in moving among the phases. Instead, the phases are simply assumed to be connected by at least one transport path with the mass transfer coefficients along this path sufficiently large to ensure equilibrium. The water in the dissolved phase is assumed to be exchanged with the vapor phase. For convenience and numerical stability, it is assumed that water *leaving* the dissolved phase passes through the vapor phase and goes directly into the liquid phase. Water *entering* the dissolved phase comes directly from the vapor phase. Water is exchanged freely between the liquid and vapor phases, thus maintaining all three phases in equilibrium.

Mass transfer among the phases and equilibrium constraints are implemented by the source terms of Eqs. (14) and (15) and switch functions given by Eqs. (37) and (38). The equilibrium between liquid and vapor phases is maintained by Eq. (14) which yields a large positive value for the term S_{LV} (corresponding to rapid evaporation) if liquid is present and the adjacent vapor exists at a pressure below saturation. Conversely, if the pressure of the vapor phase exceeds the saturation pressure, the term S_{LV} exhibits a large

Table 4
Boundary conditions

Governing equation	Anode inlet	Anode exit	Cathode inlet	Cathode exit	Comments
Momentum	$u_{y,\text{avg}} = 1547\,\text{mm/s}$	$P = P_{\text{exit}}$	$u_{y,\text{avg}} = 3747\,\text{mm/s}$	$P = P_{\text{exit}}$	–
Oxygen transport	$\nabla \cdot w_{O_2} = 0$	$\nabla \cdot w_{O_2} = 0$	$w_{O_2} = 0.21$	$\nabla \cdot w_{O_2} = 0$	Initial concentration in the anode is set to zero
Water vapor transport	$w_{WV} = 0.62$	$\nabla \cdot w_{WV} = 0$	$w_{WV} = 0.10$	$\nabla \cdot w_{WV} = 0$	–
Dissolved water transport	$\nabla \cdot c^{p}_{DW} = 0$	$\nabla \cdot c^{p}_{DW} = 0$	$\nabla \cdot c^{p}_{DW} = 0$	$\nabla \cdot c^{p}_{DW} = 0$	Initial concentration based on equilibrium with the water vapor
Liquid water transport	$s = 0$	$\nabla \cdot s = 0$	$s = 0$	$\nabla \cdot s = 0$	–
Membrane potential	$\nabla \cdot \phi_i = 0$	$\nabla \cdot \phi_i = 0$	$\nabla \cdot \phi_i = 0$	$\nabla \cdot \phi_i = 0$	–
Energy	353 K	–	353 K	–	Constant temperature BCs along the gas channels

negative value (corresponding to rapid condensation). The dissolved phase is maintained in equilibrium by Eq. (15) which transfers water from the dissolved phase to the vapor phase in proportion to the difference between the vapor density, ρ^{g}_{WV} and the density of the vapor in equilibrium with the dissolved phase, ρ^{p}_{WV}. Water evaporating from the dissolved phase passes directly through the vapor phase and into the liquid as reflected by the term $S_{WD}(1-\gamma_{WD})/\rho_{WL}$ in Eq. (5). Water enters the dissolved phase from the vapor phase as reflected by the term $\gamma_{WD}S_{WD}$ in the conservation equations for overall mass, Eq. (1) and water vapor, Eq. (4). The variable γ_{WD} is a switch term, defined by Eq. (38) that has a value of 1 when water is leaving the dissolved phase and zero otherwise. Finally, water entering or leaving the dissolved phase is reflected by the term S_{WD}/M_w in the equation for dissolved water transport, Eq. (6).[2] The mass transfer coefficients that permit exchange between the phases and the parameters for the gradual switch function, γ_{LV}, were chosen so that the three phases remain near equilibrium with one another. Numerical tests were conducted to verify that near-equilibrium conditions were maintained among the three phases and that the vapor pressure at which evaporation/condensation occurred was within ±2.5% of the saturation vapor pressure at the local temperature.

2.3. Boundary conditions

Table 4 contains the boundary conditions and the starting solution used in the model. Since the model is solved by an iterative solution technique, the choice of a starting solution can affect convergence and solution time. The starting solution for the species was set equal to their respective inlet boundary values.

[2] The term S_{WD} has dimensions of mass of water produced per unit time per unit volume, g/mm^3 s which is consistent with gas species transport Eqs. (1), (3), and (4). The liquid water transport equation is expressed in terms of fraction of the local volume filled with water so that S_{WD} must be divided by the liquid water density to yield units of mm^3-water/mm^3 s or simply s^{-1}. The dissolved water transport equation is expressed in terms of concentration so that S_{WD} must be divided by the molar mass of water to yield units of mol-water/mm^3 s.

2.4. Physical property evaluation

In addition to governing equations and boundary conditions, the numerical model incorporates a number of parameters some of which are fundamental physical properties and others which may be chosen by the fuel cell designer. Table 5 indicates values for properties such as the viscosity of the reactant gases, the exchange current density on bright platinum, etc. that are not design variables. In general, the values in Table 5 were determined from the literature. Values for the exchange current density, transfer coefficient, number of electrons in the rate limiting step, solubility of oxygen in Nafion, and the diffusion coefficient for oxygen in Nafion were estimated from data presented by Zhang et al. [19]. The estimation of these properties was required given that that data in [19] is presented over a temperature range of 303–343 K, and the base case model was run at a temperature of 353 K. In addition, the value used for the diffusion coefficient of oxygen through Nafion is about one half of that reported in [19]. This was done because the diffusion coefficient in recast Nafion is smaller than in Nafion membranes [5]. Additional properties for Nafion were taken from Zawodzinski et al. [23].

Table 6 indicates values for parameters that can be specified by the fuel cell designer. Values in Table 6 were generally determined by direct measurements or specifications for the base case fuel cell that was used for validation of the numerical model. The base case fuel cell used for validation consisted of a 5 cm^2 fuel cell assembly, carbon flow field plates, ELAT® GDLs, and a catalyzed Nafion 112 membrane. Geometric properties of the fuel cell assembly were measured directly. In the assembled cell, GDL thickness is non-uniform as it is highly compressed under the flowfield shoulders, but not under the gas channels. The thickness of the GDL was calculated as the average of the uncompressed GDL thickness and the compressed thickness, which was set by the gasket material. The porosity of the uncompressed GDL was assumed to be 0.6. This value was then adjusted to account for a decrease in void volume due to GDL compression. The tortuosity factor that modifies the gas species diffusion coefficients in the GDL was estimated from the work of Springer et al. [22].

Table 5
Physical properties

Property	Value	Source
Faraday's constant, F	96487 C/mol	[8]
Permeability of gas diffusion layer, κ^{gdl}	1.8×10^{-5} mm^{-2}	[8]
Cathode gas viscosity, μ_{air}	1.0×10^{-5} Pa s	Calc.[a]
Anode gas viscosity, μ_{H_2}	2.0×10^{-5} Pa s	Calc.[a]
Liquid water viscosity at 80 °C, μ_{WL}	4.0×10^{-3} g/(cm s)	[26]
Diffusivity of oxygen in the polymer, D_{m,O_2}	2.0×10^{-4} mm/s	Est[b]
Diffusivity of hydrogen in the polymer, D_{m,H_2}	7.9×10^{-4} mm/s	[7]
Reference anode exchange current density, i_{0,H_2}	3.0×10^{-5} A/mm^2	[27]
Reference cathode exchange current density, i_{0,O_2}	4.1×10^{-9} A/mm^2	Est.[b]
Anodic transfer coefficient, α_a	0.50	[27]
Cathodic transfer coefficient, α_c	0.55	Est.[b]
Oxygen reference concentration, $c_{O_2,ref}$	1.18×10^{-9} mol/mm^3	Est.[b]
Hydrogen reference concentration, $c_{H_2,ref}$	2.66×10^{-8} mol/mm^3	Calc.[c]
Solubility coefficient for the cathode, $h_{d,c}$	0.19	Est.[b]
Solubility coefficient for the anode, $h_{d,a}$	0.64	Calc.[c]
Entropy of reaction—anode, $s^0_{f,a}$	42.5 J/(mol K)	Calc.[d]
Entropy of reaction—cathode, $s^0_{f,c}$	126.8 J/(mol K) (liq wtr), 64.8 J/mol-K (wtr vpr)	Calc.[d]

[a] Calculated from inlet conditions.
[b] Estimated from data in [19] at a temperature of 343 K and fully humidified O_2 pressure of 1 atm.
[c] Calculated from data in [7] at a temperature of 353 K and H_2 pressure of 1 atm.
[d] Based on anode and cathode half reactions.

The catalyst layer for the base case cell was prepared using a catalyst ink composed of carbon supported catalyst (20 wt.% Pt on Vulcan XC-72R) dispersed in a 5 wt.% Nafion® 1100 solution. The fabrication technique was similar to the decal method given in Wilson et al. [20] with the exception that the ink was applied in the protonated, not TBA^+ form. The mass and composition of the catalyst layer were recorded and used to determine the volume fraction of the various constituents and the overall catalyst layer porosity. The thickness of the catalyst layer was determined from SEM images of the MEA cross-section such as the one presented in Fig. 2.

The catalyst layer porosity was determined by evaluating the solid volume of the catalyst layer based on its mass and composition and the total volume of the catalyst layer based on its thickness. The mass of the catalyst layer was determined by weighing the catalyst layer after it had been painted onto a Teflon decal and dried to remove all of the solvent. The solid volume of the catalyst layer, V_s, was then be determined by

$$V_s = \frac{m_{cat} x_p}{\rho_p} + \frac{m_{cat} x_C x_{Pt}}{\rho_{Pt}} + \frac{m_{cat} x_C (1 - x_{Pt})}{\rho_C} \quad (40)$$

where m_{cat} is the mass of the catalyst layer, x_p the mass fraction of polymer in the catalyst, x_C the mass fraction of carbon supported catalyst, x_{Pt} the mass fraction of platinum in the carbon supported catalyst, ρ_p the density of the polymer, ρ_C the density of the carbon support, ρ_{Pt} the density of platinum. The total volume of the catalyst layer including the pores, V_{tot}, can be estimated from the SEM images. From these two volumes the porosity, ε^{cat}_{void}, which is the volume fraction of pores in the catalyst layer relative to the total layer volume, can be calculated and is expressed as

$$\varepsilon^{cat}_{void} = \frac{V_{tot} - V_s}{V_{tot}} \quad (41)$$

This approach for determining porosity assumes that the Nafion and carbon phases do not coexist (i.e. the Nafion does not fill the micropores in the activated carbon). This assumption is consistent with the work of Uchida et al. [24] who concluded that the Nafion only exists in the larger pores such as those between particles or agglomerates.

Cyclic voltammetry (CV) was used to determine the active catalyst area, A_{act}, within the catalyst layer. The CV tests were conducted using an approach similar to that described by O'Hayre et al. [25]. With this approach, the electrical potential applied to the catalyst layer is varied from −0.1 to 1.0 V and back in a triangle waveform while the current is recorded. The current is integrated over time to determine the charge transferred during the adsorption and desorption

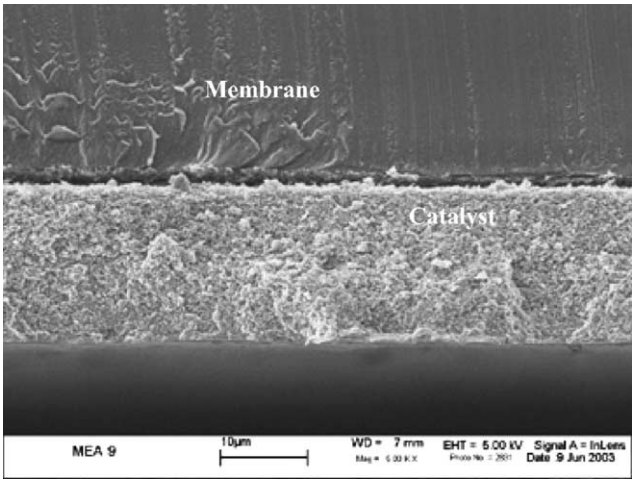

Fig. 2. SEM image of the test MEA. Magnification is 5000×.

Table 6
Design and operating parameters for validation study

Property	Value	Source
Gas channel width, W_{gc}	30.0 cm	Measured
Gas channel length, L_{gc}	1.0 mm	Measured
Gas channel height, H_{gc}	1.0 mm	Measured
Collector thickness, t_{col}	1.0 mm	Measured
Anode GDL thickness, t_{agdl}	0.290 mm	Est.[a]
Cathode GDL thickness, t_{cgdl}	0.254	Est.[a]
Gas diffusion layer void fraction, ε_{void}^{gdl}	0.375	Est.[a]
Catalyst layer thickness, t_{cat}	0.0165 mm	Measured
Pt and carbon volume fraction in the catalyst layer, ε_c^{cat}	0.45	Calc.[b]
Catalyst layer void fraction, ε_{void}^{cat}	0.31	Calc.[b]
Polymer volume fraction in the catalyst layer, ε_p^{cat}	0.24	Calc.[b]
Membrane thickness, t_m	0.0508 mm	Measured
Cell temperature, T_{coll}	353 K	Measured
Inlet pressure, P_{in}	310 kPa	Measured
Air inlet relative humidity, Rh_c	100%	Measured
Fuel inlet relative humidity, Rh_a	100%	Measured
Theoretical open circuit voltage, E_{th}	1.19	Calc.[c]
Open circuit voltage, V_{oc}	Varies	Measured
Specific reaction area of the catalyst layer, A_{v1}	6990 mm^{-1}	Measured
Mean agglomerate size, L_{aggl}	400.0 nm	Data fit[d]
Tortuosity of the GDL, τ^{gdl}	3.5	Data fit[d]
Evap./cond. mass transfer coefficient, ψ	2 g/mm^3 s	Equil.[e]
Dissolved/vapor mass transfer coefficient, h_m	5000 s^{-1}	Equil.[f]

[a] Estimated from the uncompressed thickness, void fraction, and degree of compression.
[b] Calculated from the catalyst layer composition and mass.
[c] Calculated from Nernst equation for base case reactant temperature, pressure, and composition.
[d] Property adjusted (within the range reported in the literature) to fit the data.
[e] Chosen large enough to maintain equilibrium between liquid and vapor phases.
[f] Chosen large enough to maintain equilibrium between dissolved and vapor phases.

of a monolayer of hydrogen on the active catalyst surface. The active area of the catalyst can be then be calculated from

$$A_{act} = \frac{Q_A}{Q_{Pt}} \quad (42)$$

where Q_A is the amount of charge (μC) transferred during adsorption (or desorption) and Q_{Pt} the charge transferred during the adsorption of a monolayer of hydrogen on atomically smooth platinum (210 $\mu C/cm^2$).

2.5. Numerical methods

The outer surfaces of the gas channels shown in Fig. 1 are bounded by the collector plates (not shown) and are impermeable to gases. As part of the single domain formulation, each governing equation is solved throughout the entire domain, even if the equation is not physically valid in every region. This is accomplished using a variety of numerical techniques [8,21]. For instance, to eliminate the diffusive flux of the gas species through the membrane, which is assumed impermeable to gases, the diffusivities of all gas species are set to zero within the membrane region of the model. The domain is divided into 64×121 elements. Mapped meshing is used to maintain a sufficient mesh density throughout the model domain. In regions of large gradients, such as at interfaces and in the catalyst layers, mesh size is decreased, while in the gas channels and other regions of relatively small gradients, it is much coarser. A sensitivity analysis was conducted by doubling the number of elements in the mesh. The solution changed on average by less than 2.0% and so was assumed to be mesh independent. The equations are solved with the commercial CFD solver, CFDesign®.

3. Results and discussion

The numerical model is validated by comparing model results to experimental data. The base case cell was run at a cell temperature of 80 °C with the inlet reactant gases on both the anode and cathode sides maintained at a temperature of 80 °C, a pressure of 30 psig, and a relative humidity of 100%. The mass flow rate, at both the anode and cathode, corresponded to a stoichiometric ratio of 6 at a current density of 1 A/cm^2. A comparison of model results with experimental data at 30 psig (base case) and 20 psig is shown in Fig. 3a and b, respectively.

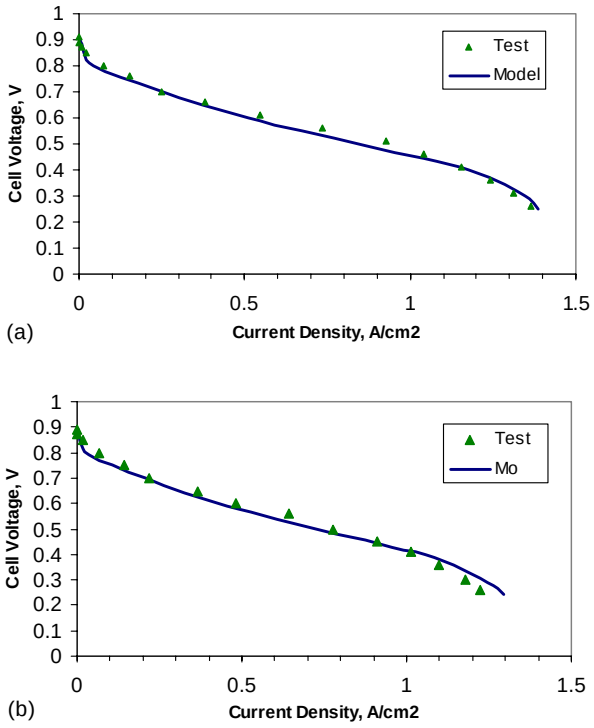

Fig. 3. (a) Model comparison with test data at 30 psig (base case). (b) Model comparison with test data at 20 psig.

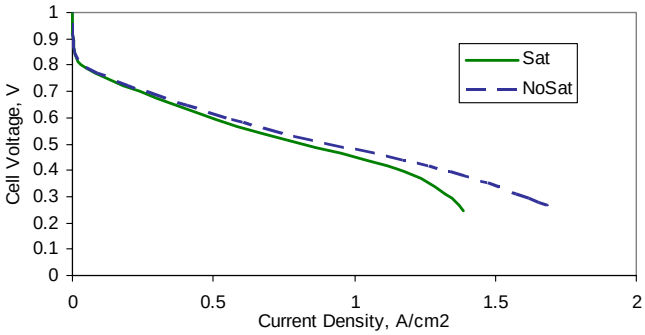

Fig. 4. Effect of liquid water buildup on cell performance.

Some of the modeling parameters were estimated by adjusting their values until good agreement was achieved between the test results and the model output. This was done only once, for the 30 psig case. The results shown in Fig. 3b for 20 psig indicate that, without further adjustment, the model is able to accurately predict performance when the cell is running under conditions that differ from the base case.

Of particular interest in Figs. 3a and b is the loss in performance due to mass transfer limitation at high current density. The increasingly steep drop in performance as the cell approaches its limiting current density is attributable to the saturation of the cathode GDL and catalyst layer with water and the corresponding restriction in reactant transport. Previous efforts [3,12] to explain limiting current behavior based solely on diffusive resistance in the agglomerates led to a more abrupt drop in performance. By including the effects of liquid water transport, the current model is able to more closely simulate performance in the region where mass transport effects begin to dominate.

The importance of liquid water transport to the accurate modeling of fuel cell performance is further illustrated in Figs. 4 and 5. Performance curves with and without liquid water transport are shown for the base case conditions in Fig. 4. The curve labeled “NoSat” does not include the effect of liquid water accumulation on gaseous reactant transport. The predicted performance when liquid water effects are neglected is much better than for the case labeled “Sat”,

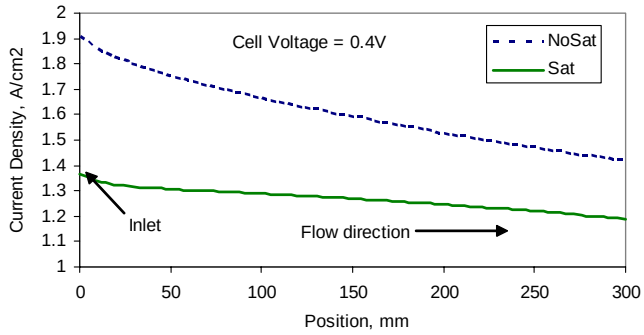

Fig. 5. Influence of liquid water on current density variation along the flow direction.

which does include the effect of liquid water accumulation on reactant transport. Comparison of the two curves demonstrates that the effects of liquid water accumulation become apparent even at relatively low values of current density. Furthermore, when liquid water effects are not included in the model, the cell voltage does not exhibit an increasingly steep drop as the cell approaches its limiting current density. This drop off in performance is clearly demonstrated by experimental data, but cannot be accurately modeled without the incorporation of liquid water transport.

The variation of current density along the channel for the same two cases at a cell voltage of 0.4 V is shown in Fig. 5. In the case where liquid water does not impede reactant transport (“NoSat”) the current density produced in the cell is greater in magnitude down the channel relative to the more physically realistic case (“Sat”). In the absence of liquid water, the drop in current density as the reactants are depleted down the channel is more pronounced. When saturation is considered, a decrease in current density in the flow direction reduces the water production rate and leads to a lower degree of saturation of the cathode GDL and catalyst layer at the exit to the cell. With less accumulated water, the GDL and catalyst layer are more open to reactant flow, thus counteracting the effect of reactant depletion and leading to more uniform current density along the gas channel.

Fig. 6 shows a contour plot of liquid water saturation for the base case conditions in the cathode GDL and catalyst layer at an average current density of 1.18 A/cm^2. The model predicts that the level of saturation decreases along the flow direction. The decrease in saturation is due to the reduced reaction rate (associated with the drop in reactant concentration along the flow direction) and a corresponding drop in the amount of water produced as well as the amount of water dragged across the membrane from the anode.

Results from the model also demonstrate the significance of water transport from the anode to the cathode by electro-osmotic drag. This water transport reduces the performance of the cell both by dehydrating the anode, thereby decreasing its conductivity, and by increasing the accumulation of liquid water at the cathode, which decreases its permeability to reactant gas flow.

Fig. 7 shows profiles for polymer water content in the catalyst layers and membrane as a function of the local current density and position through the thickness of the MEA at a point halfway down the channel for the base case conditions. The influence of electro-osmotic drag is readily apparent from these results. At low current density, there is very little change in water content across the MEA. This is due to a relatively low amount of drag and to the fact that the vapor activity at the anode and cathode is nearly identical. As current density is increased, the water content profile becomes steeper as the anode dehydrates and the cathode water content increases. The results shown in Fig. 7 also indicate that as current density increases, the total amount of water contained in the MEA decreases. This occurs because the vapor activity of the anode stream has

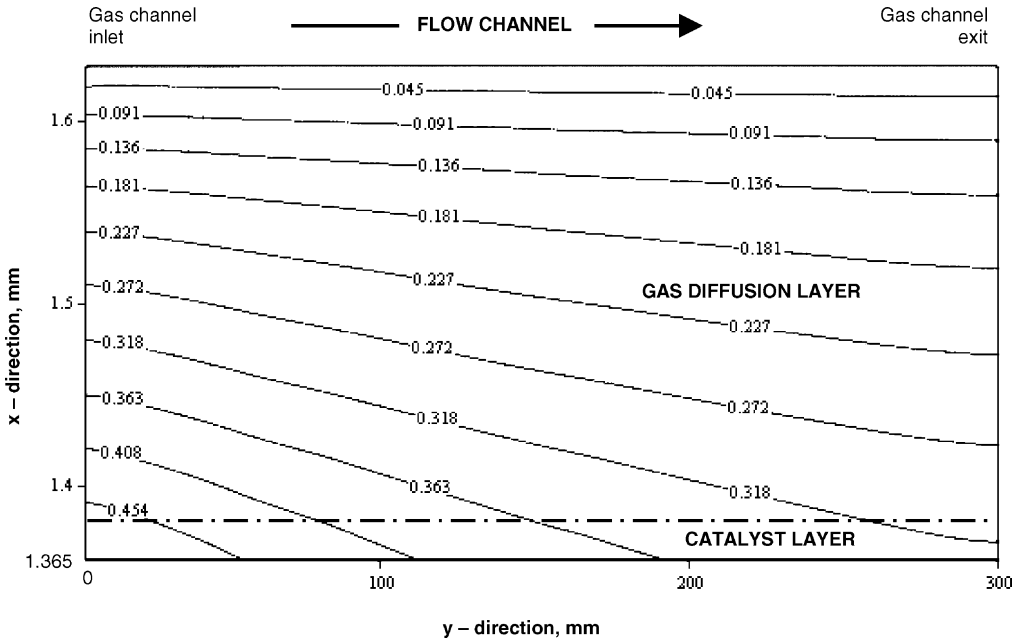

Fig. 6. Saturation profiles in the cathode.

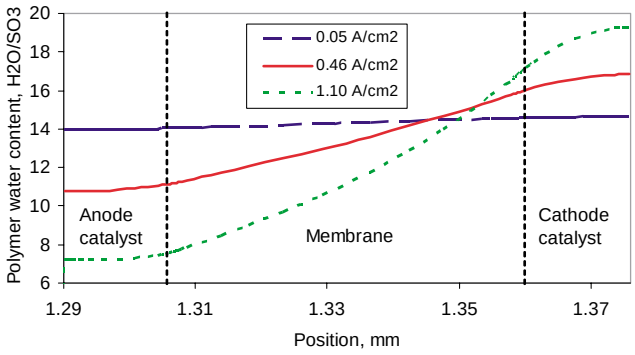

Fig. 7. Variation of polymer water content through the MEA.

dropped due to water removal upstream leaving less water available to hydrate the anode.

The effect of the water content gradient as well as the significance of the electro-osmotic drag are further illustrated by the data in Table 7. Considering electro-osmotic drag alone, the amount of water moved from the anode to the cathode for fully hydrated Nafion® would be between 2.0 and 2.9 water molecules per proton at 30 °C [23]. Due to operation with a partially hydrated membrane and catalyst layers as well as back diffusion of water from the cathode to the anode, the net amount of water moved per proton predicted by the model is between 0.16 and 0.34, which is consistent with the modeling results presented by others [6,7]. It is interesting to note that the water transported across the MEA, from the anode to the cathode, makes up between 20 and 40% of the total amount of water accumulation at the cathode (transport and electrochemical production). This indicates that in addition to limiting cell performance by way of anode dehydration, water transport by electro-osmotic drag is responsible for a significant fraction of the liquid water buildup at the cathode and the resulting reactant transport limitations.

Table 7
Water transport through the MEA

Average current density (A/cm^2)	Net water transport per proton (H_2O/H^+)	Fraction of water accumulation at the cathode due to transport across the MEA
0.05	0.16	0.24
0.52	0.34	0.41
1.18	0.30	0.37

4. Conclusions

A comprehensive, steady state, two-dimensional model including liquid water transport has been developed and validated with experimental data. Results from the model show that, in order to accurately simulate fuel cell operation, liquid water transport within the cell must be considered as it results in a loss of performance even at relatively low current density. In addition, water transport through the polymer portion of the catalyst layer and the membrane plays an important role with respect to both Ohmic losses and reactant transport restrictions at the cathode. The model predicts a net amount of water transport across the membrane of between 0.16 and 0.34 mole of water per mole of protons transported from the anode to the cathode. This accounts for 20–40% of the total amount of water accumulation at the cathode, which is a combination of water produced electrochemically and water transported by electro-osmotic drag. When operating at high inlet

humidity, any water accumulating at the cathode remains in the liquid phase and fills the porous regions of the catalyst layer and the GDL. The fraction of pores filled with liquid water is highest within the catalyst layer near the inlet to the cell.

References

[1] P.C. Sui, L.D. Chen, J.P. Seaba, Y. Wariishi, Modeling and Optimization of a PEMFC Catalyst Layer, SAE Congress, 1999-01-0539, 1999, pp. 61–70.
[2] C. Marr, X. Li, Composition and performance modeling of catalyst layer in a proton exchange membrane fuel cell, J. Power Sources 77 (1999) 17–27.
[3] K. Broka, P. Ekdunge, Modelling the PEM fuel cell cathode, J. Appl. Electrochem. 27 (1997) 281–289.
[4] D. Genevey, M.R. von Spakovsky, M.W. Ellis, D.J. Nelson, B. Olsommer, F. Topin, N. Siegel, N. Montel, Transient Model of the Heat, Mass and Charge Transfer as well as Electrochemistry in the Catalyst Layer of a PEMFC, International Mechanical Engineering Congress and Exposition—IMECE'2002, ASME IMECE Paper No. 33322, New York, NY, November 2002.
[5] F. Jaouen, G. Lindbergh, G. Sundholm, Investigation of mass-transport limitations in the solid polymer fuel cell cathode, J. Electrochem. Soc. 149 (4) (2002) A437–A447.
[6] T.E. Springer, T.A. Zawodzinski, S. Gottesfeld, Polymer electrolyte fuel cell model, J. Electrochem. Soc. 138 (8) (1991) 2334–2341.
[7] D.M. Bernardi, M.W. Verbrugge, A mathematical model of the solid-polymer-electrolyte fuel cell, J. Electrochem. Soc., vol. 139, no. 9, pp. 2477–2490.
[8] S. Um, C.Y. Wang, K.S. Chen, Computational fluid dynamics modeling of proton exchange membrane fuel cells, J. Electrochem. Soc. 147 (12) (2000) 4485–4493.
[9] V. Gurau, H. Liu, S. Kakac, Two-dimensional model for proton exchange membrane fuel cells, J. AIChe, vol. 44, pp. 2410–2422.
[10] T. Zhou, H. Liu, 3-D model of proton exchange membrane fuel cells, Proceedings ASME Heat Transfer Division HTD 366-1 (2000) 43–49.
[11] S. Dutta, S. Shimpalee, J.W. Van Zee, Numerical prediction of mass-exchange between cathode and anode channels in a PEM fuel cell, Int. J. Heat Mass Transfer 44 (2001) 2029–2042.
[12] N.P. Siegel, M.W. Ellis, D.J. Nelson, M.R. von Spakovsky, Single domain PEMFC model based on agglomerate catalyst geometry, J. Power Sources 115 (2003) 81–89.
[13] A. Parthasarathy, S. Srinivasan, A.J. Appleby, C.R. Martin, Temperature dependence of the electrode kinetics of oxygen reduction at the platinum/Nafion® interface—a microelectrode investigation, J. Electrochem. Soc. 139 (9) (1992) 2530–2537.
[14] J. Ihonen, F. Jaouen, G. Lindbergh, A. Lundblad, G. Sundholm, Investigation of mass-transport limitations in the solid polymer fuel cell cathode, J. Electrochem. Soc. 149 (4) (2002) A448–A454.
[15] W. He, J.S. Yi, T. Van Nguyen, Two-phase flow model of the cathode of PEM fuel cells using interdigitated flow fields, AIChI J. 46 (10) (2000) 2053–2064.
[16] D. Natarajan, T. Van Nguyen, A two-dimensional, two-phase, multicomponent, transient model of the cathode of a proton exchange membrane fuel cell using conventional gas distributors, J. Electrochem. Soc. 148 (12) (2001) A1324–A1335.
[17] Z.H. Wang, C.Y. Wang, Two-phase flow and transport in the interdigitated air cathode of proton exchange membrane fuel cells, Proceedings ASME Heat Transfer Division HTD 366-1 (2000) 27–33.
[18] J.J. Baschuk, X. Li, Modeling of polymer electrolyte membrane fuel cells with variable degrees of water flooding, J. Power Sources 86 (2000) 181–196.
[19] L. Zhang, C. Ma, S. Mukerjee, Oxygen permeation studies on alternative proton exchange membranes designed for elevated temperature operation, Electrochimica. Acta 48 (2003) 1845–1859.
[20] M.S. Wilson, J.A. Valerio, S. Gottesfeld, Low platinum loading electrodes for polymer electrolyte fuel cells fabricated using thermoplastic ionomers, Electrochim. Acta 40 (3) (1995) 355–363.
[21] S. Patankar, Numerical Heat Transfer and Fluid Flow, Hemisphere, Washington, DC, 1980.
[22] T.E. Springer, T.A. Zawodzinski, M.S. Wilson, S. Gottesfeld, Impedance sectroscopy, J. Electrochem. Soc. 143 (2) (1996) 587–599.
[23] T.A. Zawodzinski, T.E. Springer, J. Davey, R. Jestel, C. Lopez, J. Valerio, S. Gottesfeld, A comparative study of water uptake by and transport through ionomeric fuel cell membranes, J. Electrochem. Soc. 140 (7) (1993) 1981–1985.
[24] M. Uchida, Y. Aoyama, N. Eda, A. Ohta, Investigation of the microstructure in the catalyst layer and effects of both perfluorosulfonate ionomer and Ptfe-loaded carbon on the catalyst layer of polymer electrolyte fuel cells, J. Electrochem. Soc. 142 (12) (1995) 4143–4149.
[25] R. O'Hayre, S. Lee, S. Cha, F. Prinz, A sharp peak in the performance of sputtered platinum fuel cells at ultra-low platinum loading, J. Power Sources, 109, 483–493.
[26] R. Fox, A. McDonald, Introduction to Fluid Mechanics, Wiley, New York, 1992.
[27] J. Larminie, A. Dicks, Fuel Cell Systems Explained, Wiley, West Sussex, 2003.